SCIENCE ROBOTICS | RESEARCH ARTICLE

BIOMIMETICS

Bioinspired adaptive pupil reflex based on liquid-metal shape-shifters for machine vision

Kun Liang[1], Rui Wang[2], Gavin Lyda[1], Anran Zhang[1], Wanrong Xie[1], Yihang Wang[1], Sicheng Xing[1], Yizhang Wu[1], Zhibo Zhang[3], Yihan Liu[1], Michael D. Dickey[4], Bowen Zhu[2]*, Wubin Bai[1]*

Inspired by the evolutionary diversification of biological eyes for environmental adaptation, recently emerged artificial counterparts offer a variety of visual features that can emulate the eyes of humans, insects, fish, eagles, cats, and others. However, grand challenges reside in developing transformational artificial pupils to address drastic environmental change. Here, we propose a bioinspired vision system that integrates a hemispherical imaging array as an artificial retina with liquid-metal shape-shifters as visual neurons and an adaptive artificial pupil to comprehensively simulate visual recognition with closed-loop pupil reflex behavior. The controlled deformation of the liquid metal allows the design of a range of animal pupil shapes, and the rapid switching of short and open circuits simulates biological spike nerve signals. Under strong light, the system adaptively adjusts the pupil deformation of liquid metal to reduce the amount of exposure, which improves the image recognition accuracy of the artificial vision system under high-light conditions and confirms the key characteristics and functions of the artificial vision system, including ultrawide field of view, adaptive adjustment of light, and image recognition functions. The ability to simulate multiple shapes of animal pupils further demonstrates the programmability of the system and highlights its potential for bioinspired robotic systems, advanced machine vision, and autonomous driving.

INTRODUCTION

Evolution has led to a distinct variety of visual systems to meet the needs of diverse environments (fig. S1). These include the human eye with round pupils, optimized for a balance of focus and light regulation; the cat eye with vertical slit pupils, enhancing depth perception in low light; the sheep eye with horizontal pupils, providing a wide field of view (FoV) to detect predators; the crab compound eye, offering a panoramic perspective critical for survival in their environments; and other specialized adaptations suited to the ecological needs of different species (*1*–*4*). Recent research into these biological systems has inspired the development of advanced bionic artificial vision systems, with promising applications in machine vision, autonomous driving, drones, bioinspired robotics, and other technological fields (*5*–*14*). To facilitate multitasking across object detection, tracking, and recognition, bionic visual systems must use active perception to selectively extract salient information. These front-end capabilities are critical for facilitating robust data synthesis and real-time responsive actions. However, constantly changing environments with drastic variations in light conditions ranging from full darkness (0.01 lux or less) during the night to sun brightness (100,000 lux or more) during the day pose substantial challenges for a vision system to adapt in an automated and prompt fashion. Robust image recognition across heterogeneous illumination regimes is a fundamental requirement for the deployment of bionic visual systems. Dynamic lighting in unstructured environments attenuates target-to-background contrast and degrades boundary definition, presenting substantial challenges for reliable feature extraction and autonomous object classification.

Current machine vision systems rely on complex hardware and algorithms to achieve visual perception across a wide range of light intensities, which increases system complexity, reduces efficiency, and heightens power consumption (*15*–*17*). In contrast, the adaptive mechanism of the biological visual system adjusts dynamically through feedback from photoreceptors, neurons, and the iris, enabling it to effectively perceive and recognize objects under varying light conditions and complex backgrounds. Recent studies have integrated artificial photoelectric synaptic devices or photodetectors with actuators (*18*–*20*), simplifying the circuitry of artificial vision systems and mimicking the adaptive control exhibited by the human pupillary light reflex (PLR) (*21*). Although these bionic vision systems address issues related to circuit complexity and high power consumption, they still face challenges in achieving a wide FoV, high accuracy, and flexible adaptability for image processing and recognition across diverse environments and varying requirements.

Here, we present an artificial vision system with an adaptive pupil reflex (APR). It is based on a hemispherical flexible photosynaptic detector array with a FoV of 108°. An In_2O_3/Y6 (BTPTT-4F, a nonfullerene acceptor-donor-acceptor type small-molecular acceptor) heterojunction structure serves as the photodetector. This system exhibits ultrawide wavelength response (365 to 780 nm), spanning the ultraviolet (UV), visible, and infrared regions. In addition, under coordinated stimulation from pulsed gate voltage and anode voltage, the reversible shape-shifting of liquid metal (LM) demonstrates electrical characteristics akin to those of logic circuits. The integration of a photoelectric retina with LM (EGaIn, a eutectic gallium-indium alloy) logic modules effectively replicates the transmission of pulsed nerve signals in neurons, culminating in the successful simulation of the PLR through LM actuators' shape-shifting, enhancing image recognition performance in high-light environments. Furthermore, by leveraging the selective deformation of LM actuators, this system not only mimics the human PLR but also can be programmed to simulate the irregular pupils of various animals,

---

[1]Department of Applied Physical Sciences, University of North Carolina at Chapel Hill, Chapel Hill, NC 27514, USA. [2]Zhejiang Key Laboratory of 3D Micro/Nano Fabrication and Characterization, Department of Electronic and Information Engineering, School of Engineering, Westlake University, Hangzhou, Zhejiang 310030, China. [3]Department of Computer Science and Engineering, Michigan State University, East Lansing, MI 48824, USA. [4]Department of Chemical and Biomolecular Engineering, North Carolina State University, Raleigh, NC 27606, USA.
*Corresponding author. Email: zhubowen@westlake.edu.cn (B.Z.); wbai@unc.edu (W.B.)

including cats, sheep, cuttlefish, and frogs. This artificial vision system, with its strong tunability and adaptive feedback capabilities, demonstrates the feasibility of simulating complex, collaborative physiological behaviors involving multiple neural systems and effectors. It offers foundational strategies for neuromorphic electronics and bioinspired robotics, highlighting the potential of machine vision to address challenges posed by harsh light conditions and dynamic environmental changes in future applications.

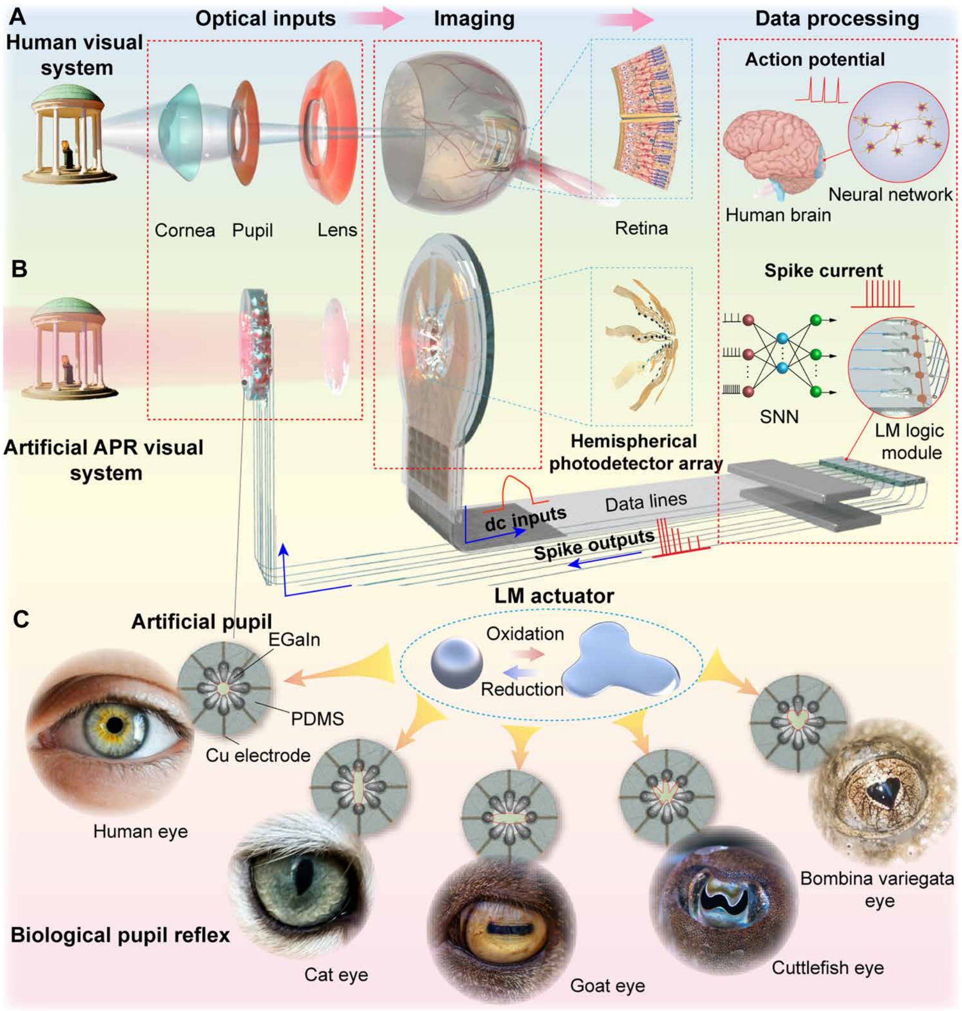

Fig. 1. Bioinspired reconfigurable artificial eye. (**A**) The biological visual system encompasses various physiological processes, including visual recognition and the PLR, which involve optical input, imaging, and data processing. Retinal neurons work in conjunction with various muscles to regulate pupillary activity, ensuring clear image formation and accurate perception in the brain. (**B**) Correspondingly, the artificial APR visual system consists of an artificial pupil, lens, hemispherical photodetectors, and artificial neurons, which work together to adaptively regulate the amount of light entering through the artificial pupil. (**C**) Over evolutionary time, diverse pupil shapes have emerged in animals, enhancing their survival in competitive and challenging environments. LM can be actively deformed through the interplay of surface tension gradient and electrostatic attraction during electrochemical reactions, emulating various pupil shapes under feedback from photoelectric synapses, thereby dynamically improving image recognition accuracy in high-exposure environments.

RESULTS

Bioinspired design of adaptive vision system

Adaptive artificial vision systems often draw inspiration from biological counterparts, which typically consist of an eyeball for optical sensing, millions of nerve fibers connected to a retina for data transmission, and a brain for data processing to enable visual recognition and the pupillary reflex (Fig. 1A). Human vision relies on tens of millions of specialized cells in the retina, including photoreceptors (rods and cones) and horizontal cells (*22*, *23*). The retina captures visual information and converts it into electrical signals, which are then transmitted to the visual cortex in the brain for processing (*23*–*26*). The pupil is a small aperture in the center of the iris that allows light to enter the eye. It is controlled by two sets of smooth muscles, as shown in fig. S2: the circular pupillary sphincter muscles, which constrict the pupil, and the radial pupillary dilator muscles, which cause it to dilate. The ability of the pupil to dilate or constrict plays a crucial role in regulating the amount of light entering the eye (*2*, *21*). In response to changes in light intensity, the pupil reflexively adjusts its size, enabling adaptation to various environmental conditions. The shape of an animal's pupil is influenced by factors such as the optical properties of the vitreous body, the shape and sensitivity of the retina, and the specific environmental and behavioral needs of the species. Although most animals have round or slit-shaped pupils, some aquatic species have pupils with more distinctive forms. The optical properties of these different pupil shapes vary, enabling animals to better adapt to their respective ecological niches, improving survival and enhancing predation success (*1*, *2*, *11*).

Figure 1 (A and B) compares the human eye with the adaptive artificial vision system, which includes a lens, an EGaIn artificial pupil, a hemispherical array of photodetectors, data lines, and EGaIn artificial neurons. These components emulate the lens, pupil, retina, nerve fibers, and neurons in the brain responsible for processing visual information. The core components of the system are the hemispherical artificial retina, artificial neurons, and the artificial adaptive pupil, which consist of an In_2O_3/Y6 photodetector array, LM logic modules, and LM actuator, respectively. The hemispherical shape of the system simplified the optical structure, facilitated an expanded FoV, reduced optical aberration, and provided a broad visual perception of the surrounding environment (*27*). The dc sensed by the photodetectors, in coordination with pulsed gate voltage, regulates the deformation of the LM logic module (*28*–*31*), generating spike currents with frequencies dependent on light intensity. These currents are then used to programmatically drive the deformation of the LM actuator, simulating various biological pupillary reflexes controlled by iris

PHOTO CREDITS: CUTTLEFISH EYE, PEXELS; HUMAN EYE, SHEEP EYE, AND BOMBINA VARIEGATE EYE, PIXABAY; CAT EYE, COURTESY OF K.L.

muscles (Fig. 1B). This enables effective modulation of light intake, adapting to different light conditions and visual requirements (Fig. 1C).

Fabrication and optoelectronic performance of the artificial retina

Inspired by the human eye, we developed an artificial retina consisting of a hemispherical photodetector array with an integrated structure that uses parylene as the supporting substrate, In_2O_3/Y6 as the light-sensing units, gold (Au) as the conductive traces, and an epoxy-based insulative negative photoresist (SU8) as the encapsulation (Fig. 2, A to G). A more detailed description of the fabrication process appears in Materials and Methods and in figs. S3 and S4. This device architecture exhibited superior performance in mechanical bending and twisting without interference to its functionality (fig. S5). As displayed in Fig. 2 (C and F), the flexible imaging array consists of 64 photodetectors in total, which are evenly distributed across eight branches with a separation angle (α, defined in Fig. 2C) of 45°. Next, the imaging array was affixed to a prestretched Ecoflex substrate, and the subsequent release of the stress buckled the imaging array into a three-dimensional (3D) hemispherical architecture with a diameter of ~1.1 cm (Fig. 2, D and E, and fig. S4). The resultant hemispherical design of the imaging array offered enhanced focusing of objects onto each pixel, thereby widening the FoV, as illustrated in Fig. 2C. Furthermore, fig. S6 shows a comparison of the FoV calculations between the hemispherical imaging array and the planar counterpart in their projected planar shapes. The hemispherical device achieved a FoV of up to 108°, substantially wider than its planar counterpart (~68°).

The thicknesses of solution-processed In_2O_3 and Y6 films were ~9.0 and 18.0 nm, respectively, as depicted in the height profiles from atomic force microscopy (AFM) images (fig. S7). The UV–visible (vis) absorption spectra of In_2O_3 and Y6 films are shown in Fig. 2H. Y6 (BTPTT-4F), an established nonfullerene acceptor molecule, exhibited broad absorbance with a peak around 800 nm, whereas the In_2O_3 films displayed higher absorbance at wavelengths below 400 nm. Tauc plot analysis provided an estimate for the bandgap energy (E_g) values of In_2O_3 and Y6 to be 3.77 and 1.32 eV, respectively (fig. S8, A and B). Figure S8C shows the ultraviolet photoelectron spectroscopy (UPS) spectra of the valence bands of the In_2O_3 and Y6 films. The valence band maximum (VBM) was measured to be 1.15 eV for the Y6 sample and 3.00 eV for the In_2O_3 sample with respect to the Fermi level (E_F). Therefore, the energy band alignment between the In_2O_3 and Y6 layers was constructed on the basis of the Tauc plots and the UPS analysis, as presented in Fig. 2I, which demonstrated the formation of a heterojunction. According to the band diagram analysis, the conduction band minimum of In_2O_3 was higher than that of Y6 by around 0.6 eV at the heterojunction interface, whereas the difference between their VBMs was as high as 1.85 eV, which suggested that the electrons generated during exposure to the near infrared (NIR) and visible light can be easily transferred to the conduction band of the underlying In_2O_3 film (*24*, *25*, *32*). As a metal oxide semiconductor, In_2O_3 exhibits high carrier mobility, which facilitates charge carrier transportation (*33*–*35*). The ionization of oxygen vacancies is widely recognized as the primary mechanism responsible for persistent photoconductivity (PPC) in metal-oxide semiconductors, which is a defining characteristic of bioinspired synaptic devices (*36*). These oxygen vacancies exist in shallow donor states (Vo^+ and Vo^{2+}) and deep localized states (Vo) in the oxide material (*37*, *38*). As illustrated in Fig. 2I, UV illumination substantially promoted oxygen vacancy ionization, generating excess electrons. This process released additional charge carriers into the In_2O_3 matrix, thereby enhancing its conductivity. Subsequently, the conductivity underwent gradual decay through the recombination and neutralization of Vo^+ and Vo^{2+} species.

Figure 2J shows the photocurrent of an In_2O_3/Y6 photodetector under NIR, red, green, blue, and UV light pulses for the same light intensity (≈0.8 mW/cm^2), which revealed a broadband response. Exposure to 365- and 450-nm light induced substantial ionization of oxygen vacancies in In_2O_3 film, leading to pronounced PPC effects and manifesting long-term plasticity. In contrast, under 520-nm light stimulation, the device exhibited short-term plasticity, whereas 650- and 780-nm illumination elicited faster photodetection responses (*32*, *37*–*39*). The corresponding response times, as shown in fig. S9, demonstrated its multimodal operational capability across distinct spectral regions. Figure S10 shows representative current-voltage (*I*-*V*) characteristics of an In_2O_3/Y6 photodetector, as measured both under dark and illuminated ($\lambda = 650$ nm) conditions using laser light at various powers (0.4 to 52.1 mW/cm^2). Figure 2K displays the photocurrent response to an on/off switching cycle over time, whereas fig. S11A shows the corresponding photocurrent response at higher frequencies. The In_2O_3/Y6 photodetector achieved a faster response time of <20 ms when the light power surpassed 50 mW/cm^2 (fig. S11B). The observed repeatable and fast switching characteristics demonstrate remarkable photocurrent reproducibility. The relationship between photocurrent and optical power density is illustrated in Fig. 2L.

In addition, the photodectectors were also evaluated using responsivity (*R*), detectivity (*D**), and linear dynamic range (LDR). Figure 2M shows the photocurrent density and *R* as a function of optical power density at 650-nm light illumination. When the illumination power density was reduced to 0.4 mW/cm^2, the *R* reached 1.85 mA/W, demonstrating its high sensitivity in low-light environments. Figure S12 (A and B) presents the wavelength dependence of *D** and LDR; their maximum values were 4.3×10^{10} Jones and 42.4 dB, respectively. The flexible In_2O_3/Y6 photodetector achieved an LDR comparable to that of conventional rigid InGaAs photodetectors (66 dB) (*40*). Details and relevant formulas regarding the calculation of the *R*, *D**, and LDR values appear in Supplementary Methods. We also assessed the bending stability of the photodetector array. As shown in fig. S13, when the bending radius of the artificial retina was ≥0.5 cm, more than 85% of the initial light response was retained, demonstrating superior operational stability.

The artificial retinal imaging system, depicted in Fig. 3A, comprises a lens and a hemispherical photodetector array. Figure 3B demonstrates the FoV of the hemispherical photodetector. The image-sensing functionality was evaluated by projecting an optical pattern onto the artificial retina, which subsequently records the photocurrent from each sensor pixel. As shown in Fig. 3C, the letter patterns U, N, and C projected onto the artificial retina were resolved. Because of the PPC effect, increased UV light exposure resulted in the generation of more charge carriers by the photodetector, leading to slower photocurrent recovery times (Fig. 3D). This phenomenon demonstrated the device neuromorphic visual memory capabilities. In the human brain, synaptic memory can be readily categorized into two distinct types according to the retention time: short-term memory (STM) and long-term memory (LTM), both of which are considered manifestations of synaptic plasticity (*41*). As observed in Fig. 3E, the memory retention time of the C pattern exceeded 20 s after 10 cycles of UV irradiation, with a substantial increase in visual memory compared with a single exposure. Similarly, the transition from STM to LTM could be effectively emulated by modulating the intensity and frequency of optical pulses (fig. S14). Both photocurrent and decay time demonstrated a positive correlation with increasing pulse intensity and frequency.

Artificial neurons based on an LM logic module

In addition to the photosensitive system centered in the retina, the human visual system also includes neural processing units. After the photoreceptor cells perceive visual input, the optic nerve transmits the visual information as electrical impulses to the visual cortex in the brain for further processing and encoding. LM, a eutectic alloy that remains liquid at room temperature, exhibits properties such as high fluidity and superior conductivity. In contrast with conventional conductive materials, LMs can be manipulated by external stimuli (such as electrical or chemical), enabling them to transition or move between different forms, with substantial potential for applications in bionic systems and neural devices (*29*, *31*, *42*).

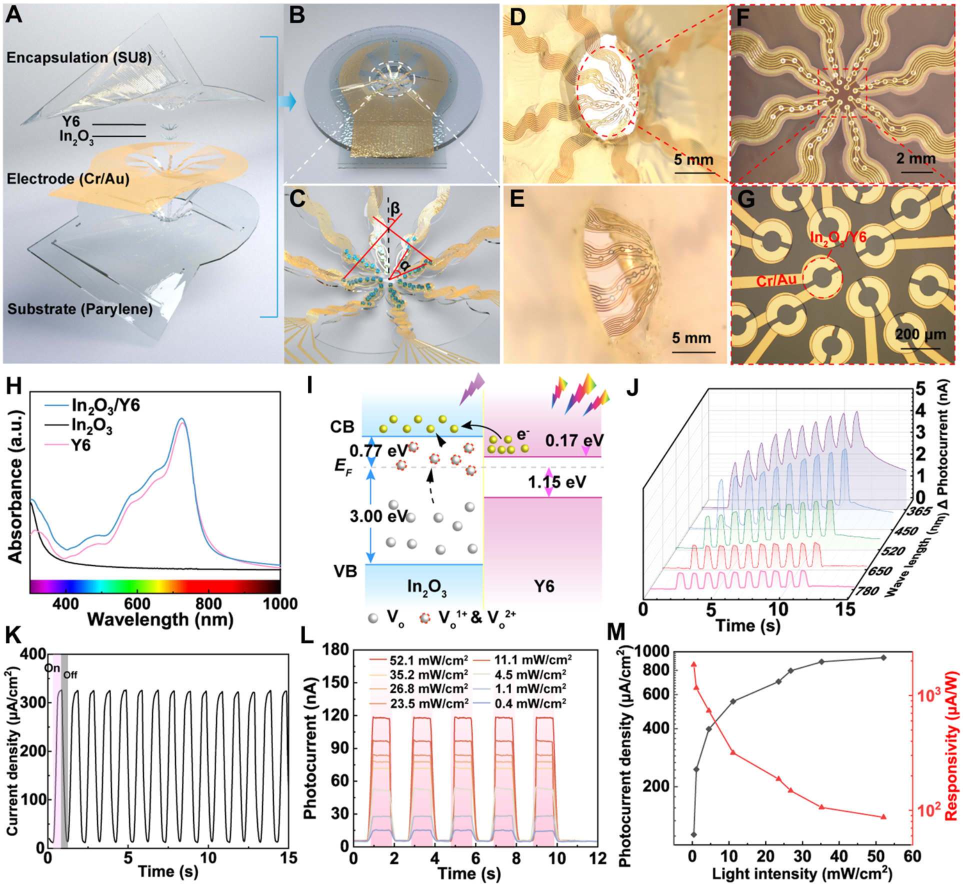

Fig. 2. 3D hemispherical artificial retina. (**A**) Exploded view of the hemispherical artificial retina. (**B**) Macroscopic schematic diagram of a fabricated artificial retina. (**C**) Structure diagram of the hemispherical photodetector array. (**D** and **E**) Side-view experimental photographs of hemispherical optoelectronic synapses. (**F** and **G**) Microscopic images of the flexible artificial retina. The sensory area is composed of a photodetector array using In_2O_3 and Y6. (G) and (F) are the enlarged detailed views of the dashed boxes in (F) and (D), respectively. (**H**) UV-vis absorption spectra of the In_2O_3, Y6, and In_2O_3/Y6 films deposited on quartz substrates. a.u., arbitrary units. (**I**) Schematic band-alignment energy diagram of In_2O_3/Y6 indicates the relative energy position of the E_F (Fermi level), CB (conduction band), and VB (valence band). (**J**) Illumination, with a pulse frequency of 1 Hz and a total of 10 pulses, of light with wavelengths from 365 to 780 nm triggers corresponding photocurrents of one photodetector. (**K**) Time-dependent on/off switching behavior under 0.1-V bias voltage with a 650-nm pulsed light. (**L** and **M**) Experimental measurement of photocurrent, photocurrent density, and responsivity dependence of 650-nm light pulses with different incident powers. The bias voltage applied to all devices was 0.1 V.

Several innovative LM-based electronic devices have been proposed, including electronic switches and logic components (*31*, *43*, *44*). These devices primarily rely on the movement of the LM—such as convergence, separation, and migration—which allows for the representation of binary electrical states (0 and 1). In air, EGaIn tends to form a thin native oxide layer on its surface, which can be dissolved by an alkaline solution (such as NaOH) (*28*). This dissolution promotes the formation of spherical droplets, driven by large surface tension, as schematically displayed in fig. S15 (A and B). However, applying a positive potential enhances oxide deposition on the surface of the EGaIn, substantially lowering the effective surface tension (*28*, *29*, *31*, *45*). This results in the flattening of the metal droplet under gravity, as depicted in fig. S15C.

Electrical spike signals, resembling biological nerve signals, were simulated by the LM logic modules (artificial neurons), as shown in Fig. 4A and movie S1. The LM logic module comprised a cathode, anode, and gate electrode, with EGaIn in NaOH solution serving as the conductive medium, as shown in stage i; the circuit was open at this stage (logic 0). When a negative voltage (≤−0.5 V) was applied to the cathode, along with a ±2-V, 1-Hz square wave voltage applied to the gate, EGaIn migrated toward the cathode under the combined influence of electrostatic attraction and surface tension gradients during stage ii, namely, the Marangoni effect (*28*, *30*, *45*). However, the wetting behavior of EGaIn on the Cu electrode surface ensured that LM adheres strongly to the anode electrode (*46*–*48*). During this process, the circuit generated a tiny pulse current (I_{cathode}) that remained well below the threshold. At stage iii, when the LM made contact with the counterelectrode, the circuit was switched on and the maximum current was generated, surpassing the threshold (logic 1) (*31*, *43*, *44*, *49*). Upon contact, partial positive charges in EGaIn were discharged, causing the electrostatic attraction to vanish instantly. Simultaneously, the positive pulse gate voltage drove the reduction of the oxide layer on the EGaIn surface, and the substantial surface tension caused the LM to contract and detach from the cathode electrode, thereby returning the system to the 0 electrical state (stage iv). When the voltage applied to the anode exceeded 3 V, the thicker oxide layer on the LM and the increased hydrogen bubbles at the cathode enabled the LM to wrap around the cathode without short-circuiting (*50*), as illustrated in fig. S16.

Increasing the operating voltage resulted in more frequent contact between the LM and the counterelectrode, as depicted in Fig. 4B. Furthermore, the LM-based logic module exhibited negligible

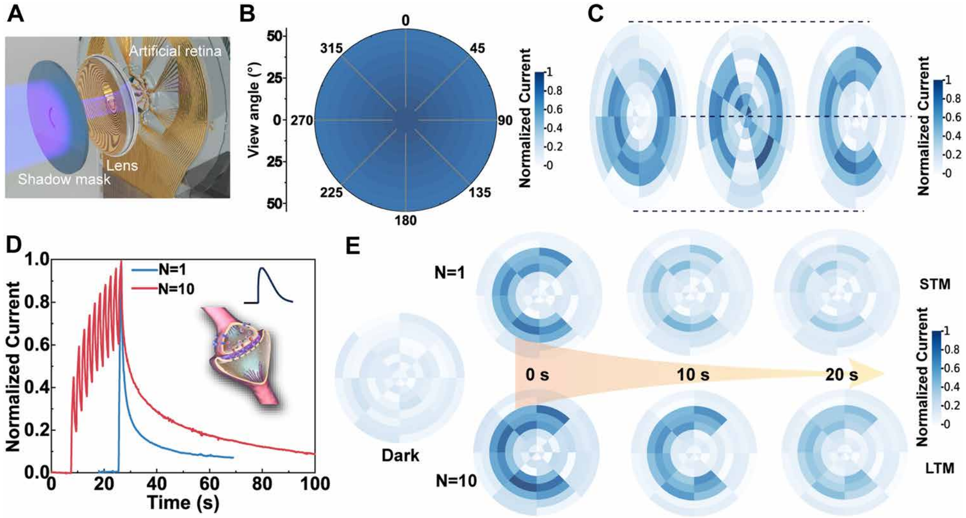

Fig. 3. Visual information perception-memory processing system based on a hemispherical artificial retina. (**A**) Schematic illustration of the hemispherical artificial retina. UV light passes through the letter-patterned mask and lens, and U-, N-, or C-shaped light is projected onto the hemispherical artificial retina, where the photodetectors at the letter position were continuously stimulated with UV light. (**B**) Schematic diagram and test results of the FoV of the hemispherical artificial retina. (**C**) Demonstrations of the hemispherical photoelectric synaptic array sensing images of the letters U, N, and C under 3.8 mW/cm^2 UV light. (**D**) Attenuation of normalized channel conductance change recorded after UV pulses (1 Hz, 3.1 mW/cm^2) with varying pulse number (*N*) at constant light intensity and frequency. This curve closely resembles that of the biological synaptic neural signals depicted in the illustration. (**E**) Hemispherical photoelectric synapses simulate learning and memory behavior, with increased learning opportunities enhancing image memory retention.

performance degradation after outputting a pulsed current for 1000 s (1000 switching cycles; fig. S17), demonstrating superior operational stability. Building on this characteristic, we designed a circuit to simulate neuronal function (Fig. 4C). The LM logic module functioned as a quasitransistor to control the on/off states of the circuit. The photocurrent generated by the photodetector was converted into voltage (*51*), amplified by the amplifier, and applied to the electrode to produce a series of spike currents ranging from 0.13 to 1 Hz, corresponding to varying light intensities (Fig. 4, D and E). This enabled the artificial vision nervous system to perceive, encode, and recognize visual information. Moreover, the expansion speed of the LM was also related to the channel width and the volume of the LM (*43*). As shown in fig. S18 (A and B), the expansion of the LM exhibited volume- and channel-dependent acceleration. An increase in LM volume and channel width promoted the expansion of oxide domains, thereby enhancing the surface tension gradient and ultimately increasing the expansion speed and frequency. Specifically, when the channel width was 3 mm (with an LM droplet diameter of 5 mm), the LM expansion speed increased from 2.3 to 10.1 mm/s as the applied voltage rose from 0.5 to 5 V. However, when the channel width was reduced to only 0.6 mm, a 0.5-V bias voltage failed to drive LM expansion because of insufficient surface tension. This suggests that, in practical applications, LM could be easily controlled by adjusting device parameters, providing tunable electrical stimulation options.

Machine vision based on the APR vision system

The mammalian visual system relies on two classical photoreceptor types in the retina: cones and rods. These conventional photoreceptors constitute the photosensitive core of the image-forming visual pathway, responsible for phototransduction (converting light signals into neural electrical signals) and subsequent transmission to the brain for visual information processing. In contrast, the PLR is mainly mediated by non–image-forming photoreceptors (NIFPs) in the retina, namely, the intrinsically photosensitive retinal ganglion cells [Fig. 5A(i)] (*52*, *53*). These specialized neurons serve as the primary afferent sensors for this reflex arc and directly regulate the pupillary constrictor muscles. Functioning as initial receptors for the PLR, these specialized neurons relay signals through sympathetic and parasympathetic pathways to modulate iris musculature, stimulating either the pupillary dilator or sphincter muscles to regulate pupil dilation and constriction. PLR refers to the change in pupil size in response to variations in light intensity, and it is a type of neural reflex. The PLR is a crucial physiological response of the eye to changes in light, playing a vital role in regulating the amount of light entering the eye, protecting the retina from excessive light exposure, and ensuring that images projected onto the retina are sharp. This reflex is essential for maintaining normal visual function. Accordingly, we defined NIFPs and image-forming photoreceptors (IFPs) on the bionic retina: The NIFPs drive LM actuators to simulate the PLR, with its light intensity–modulated pulse frequency enabling information preprocessing and encoding, whereas the IFPs are used for imaging [Fig. 5A(ii)]. The photocurrent generated by NIFPs triggers the expansion of LM in the bioinspired pupil, dynamically modulating its diameter in a feedback-controlled manner, as illustrated in fig. S19A. This mechanism replicated the biological PLR. The corresponding circuit architecture for signal processing and data acquisition is detailed in fig. S19B.

All components of the adaptive artificial vision system, namely, the pupil, lens, and photoelectric retina, are fixed at the same level, enabling precise alignment of the biomimetic pupil with the artificial retina via an alignment platform (fig. S20). The photocurrent generated by the NIFPs was converted into voltage through an amplifier, which drove the artificial neuron to generate spike currents. These currents were then converted back into voltage by the amplifier to drive the expansion of the LM actuator. Figure 5B presents the schematic diagram of the artificial APR visual system. The semiconductor parameter analyzer served as a dc power source and data acquisition system, whereas the waveform generator drove the artificial neurons, and the data were transmitted to a computer for further processing and analysis (fig. S21). The LM-based artificial pupil was placed atop the photodetector array and lens, as shown in Fig. 5C. Initially, the spherical EGaIn in NaOH was uniformly distributed around the photodetector array, analogous to the maximum dilation of the pupil in a biological eye in a dark environment [Fig. 5C(i)]. Upon application of photovoltage, electrochemical reactions caused the LM actuator to deform and expand in the polydimethylsiloxane (PDMS) channel, resulting in a reduction of the light transmission area and simulating the pupil reflex behavior of biological eyes [Fig. 5C(ii)]. Movie S2 shows the full APR activity of the system exposed to intense light. The adaptive photocurrent dynamic changes in the artificial retina after pupil reflex are shown in Fig. 5D. NIFPs were obstructed by the expanding EGaIn, which limited their exposure to light and resulted in a decrease in photocurrent (fig. S22). Consequently, the spike current frequency of the artificial neurons was also reduced (Fig. 5E), and we defined this feedback behavior as the APR, with the corresponding frequency-time evolution profile shown in fig. S23. Variations in pupil diameter and transmitted light intensity during this APR process are shown in fig. S24. The LM, actuated by voltage from the logic module, expanded in the PDMS microchannels to reduce the artificial pupil aperture size. This opto-mechanical response progressively attenuated incident light intensity until the system reached equilibrium. According to the International Electrotechnical Commission guidelines, visible light below ~10 mW/cm^2 (exposure time: 1 ms) is safe and comfortable for human eyes (*54*). Exceeding this threshold (overexposure) may cause temporary visual impairment, and prolonged exposure risks retinal damage. Noon sunlight intensity reaches tens to 100 mW/cm^2. Consequently, in Figs. 5 (C to E), light intensities up to 35.2 mW/cm^2 were applied to drive the APR system's adaptation from harsh to comfortable illumination levels (4.6 mW/cm^2), simulating maximal pupil contraction induced by excessive light exposure.

To systematically investigate the impact of bioinspired pupil dynamic variation on imaging performance in our system, we first used ray-tracing simulations to evaluate the optical effects under different pupil diameters (d_{pupil} = 1.1 cm, 0.6 cm). As demonstrated in fig. S25 (A and B), the larger pupil aperture enables enhanced light throughput but reduces depth of field (DoF) and pronounced distinct circle of confusion. Conversely, the smaller aperture achieved greater DoF at the expense of light intake, ensuring higher image quality, which matched the characteristics of biological vision and commercial camera equipment. To validate these optical characteristics and focusing performance, we measured objects at different distances (20, 30, 40, 50, and 60 mm) using two aperture types (d_{pupil} = 1.1 and 0.6 cm), as shown in fig. S26. Consistent with the commercial camera imaging results (fig. S26B), the small-pupil (*f*/16) APR vision system produced clear cross-shaped object images across the 30- to 60-mm range. In contrast, the large-pupil (*f*/2) APR system achieved a clear image only at 40 mm (fig. S26C). Consequently, vision systems using smaller pupils outperformed those with larger pupils in terms of object recognition accuracy over extended distance ranges (fig. S26D). Figure S26E demonstrated the imaging performance of the APR vision system during adaptive pupil dynamics, with recognition accuracy substantially increasing as the pupil size adaptively decreased (fig. S26F).

To evaluate the potential of APR for enhancing image recognition in artificial visual systems, we constructed a spiking neural network (SNN) to identify numbers from overexposed images. The SNN comprises 784 input neurons, 196 hidden neurons, and 10 output neurons. We used the Modified National Institute of Standards and Technology (MNIST) dataset as the training set to evaluate the image recognition accuracy (handwriting digit numbers from 0 to 9), with 150% simulated noise added to mimic overexposure caused by high light intensity. After passing through the APR, the background noise of the digit was filtered out effectively and

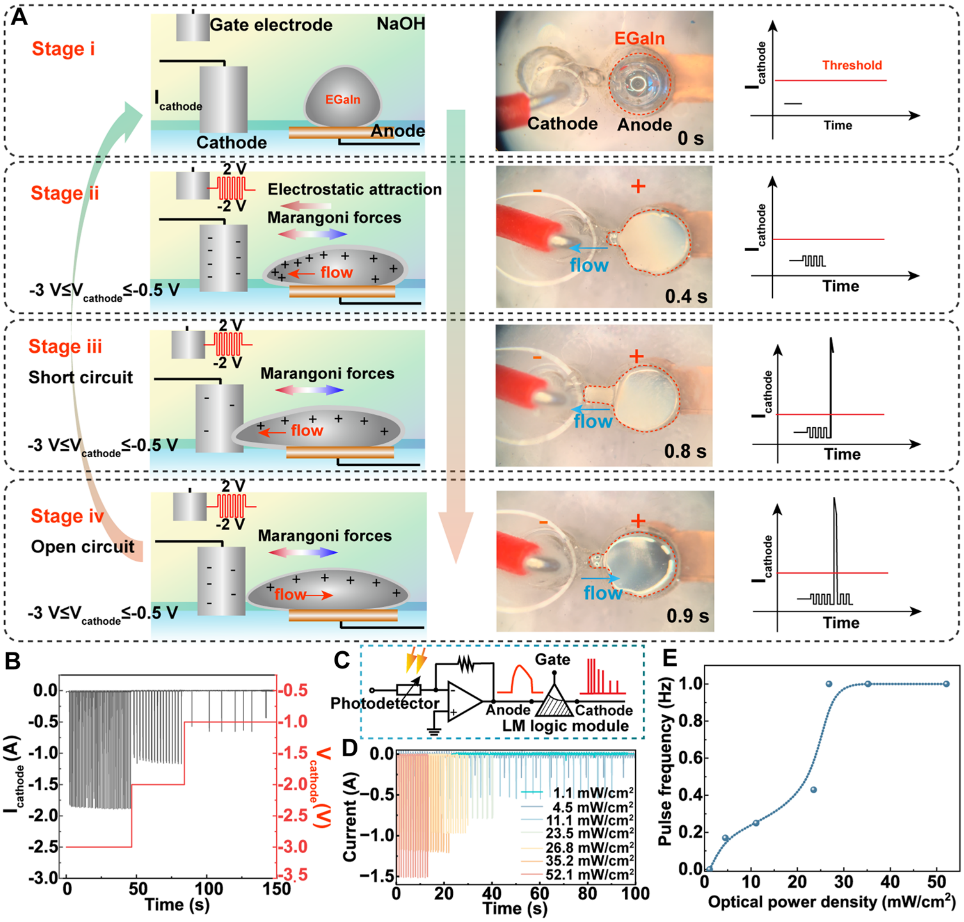

Fig. 4. Artificial neural design based on deformation of an EGaIn logic module. (**A**) Artificial nerves based on pulsed nerve signals can be constructed using an LM logic module. The system comprises a gate electrode, an anode, a cathode, and a connecting channel. LM is deposited on the anode, and the remaining cavity is filled with 0.5 M NaOH solution. The anode and cathode are positioned on opposite sides of the channel, with the gate electrode located externally. The output of artificial neural spike signals is influenced by the deformation of the LM, which is caused by the combined effect of electrostatic attraction and surface tension gradient induced by the gate pulse voltage. Upon stimulation with a pulse current, the LM successively goes through the four stages of balance, expansion, contact, and contraction. (**B**) Effect of cathode voltage on the frequency of output spike current. Higher potentials can induce greater surface tension gradients and electrostatic attraction in the LM, resulting in faster switching frequencies. (**C**) Schematic diagram of logic circuit of photoelectric synapses and neurons that convert photocurrents into spike currents. (**D** and **E**) Measured dependence of output spike current on light intensity; the gate is applied with a pulse voltage of 1 Hz, and the high and low levels are 2 and −2 V, respectively. The channel width is ~1.3 mm.

contrast was substantially enhanced (Fig. 5F and fig. S27), as in the simulated photo result (fig. S28). The denoising procedure is detailed in Supplementary Methods. Recognition rates of MNIST images before and after APR preprocessing are compared in Fig. 5G. A distinct improvement in the recognition rate with the APRs for the image preprocessing was achieved, and the recognition rate (100 epochs) was substantially improved from 68.38 to 83.56% after the image preprocessing. In addition, the confusion matrix was used to represent the progressive learning process in the SNN, as shown in Fig. 5H. As the training phase increased, the maximum inferred output value of each row gradually conformed to the desired output value of each column, suggesting that all numbers from 0 to 9 could be well identified. The processing framework integrated neural encoding techniques with an SNN model, with complete implementation details provided in Supplementary Methods and fig. S29.

The core of autonomous driving now includes sensor systems and algorithms, with cameras serving as crucial visual sensors for performing a range of image recognition and processing tasks. However, in scenarios involving object tracking, detection, and recognition, these tasks are often conducted in noisy backgrounds and complex environments, such as driving against the Sun's glare or being exposed to high-beam headlights. Under backlight conditions, cameras and other sensors struggle to accurately detect obstacles and pedestrians on the road (fig. S30). As a result, the autonomous driving system requires additional time and computational resources to process image data, potentially leading to delayed response times. This delay may hinder the system from making timely and accurate decisions, thereby increasing the risk of collisions. The APR visual system can offer inherent hardware-based advantages, substantially reducing computational load while enhancing the system's real-time performance and stability. The object detection and tracking capabilities of the system were demonstrated using the You Only Look Once v5 algorithm, with pretrained weights from the Common Objects in Context model (*10*, *55*). As illustrated in Fig. 5 (I and J), the vehicle image recognition results for several successive frames extracted from the movie also indicated that, under unfavorable optical conditions such as uneven light or overexposure, the APR system can still provide high-quality images for accurate object detection. Conversely, transition from bright to dark environments triggered dilation in contracted biological pupils. In this scenario, the APR system maintained constant transmitted light intensity throughout this process (fig. S31A), given that the bionic pupil stabilized light transmission during state transitions from constriction to dilation. Simulation results using dashcam footage (fig. S31, B and C) depicted a vehicle traversing a tunnel. When outside the tunnel, overexposure in original images yielded marginally lower confidence scores compared with APR-processed images. In the tunnel, confidence levels became comparable because of deactivation of the APR system under low light intensity.

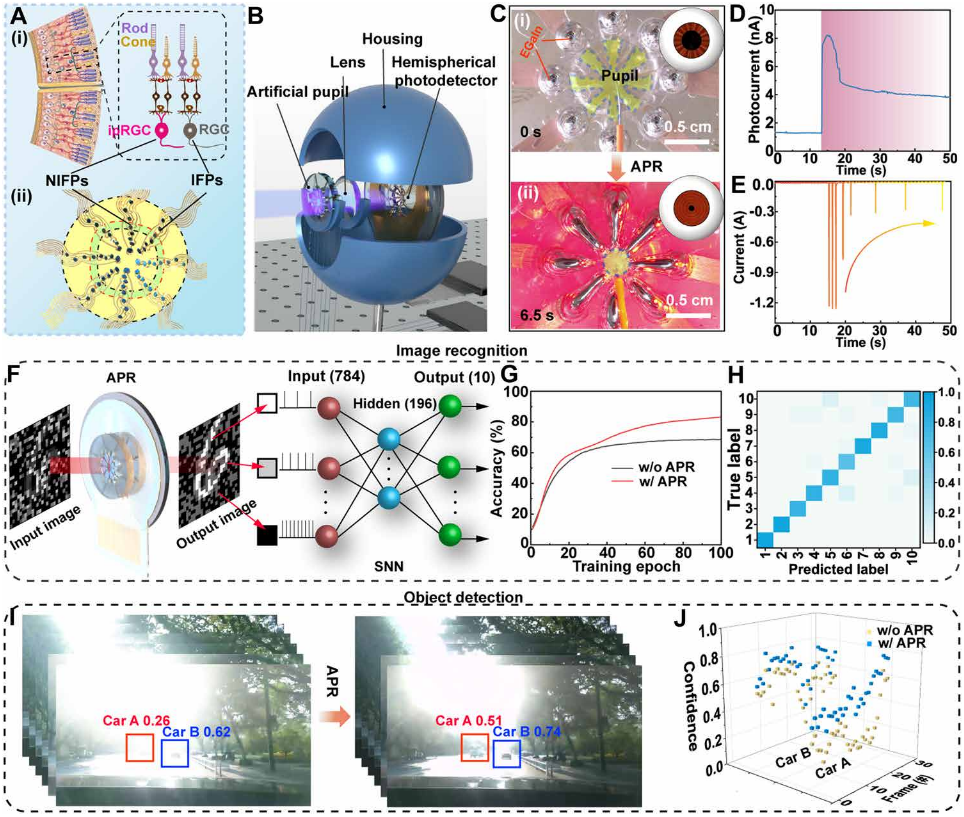

Fig. 5. APR visual system in machine vision. (**A**) Definition of NIFP and IFP regions on a photodetector array mimicking the biological retina. ipRGC, intrinsically photosensitive retinal ganglion cell. (**B**) Schematic illustration showing the artificial APR visual system. (**C**) Photograph showing the APR. The photodetector array is arranged in the green-patterned region, representing the effective pupil, with a channel width of ~1.3 mm. The inset shows a schematic plot of a human eye. (**D**) Change in photocurrent of the photodetector under the APR (650 nm, 35.2 mW/cm^2, $V = 0.1$ V). (**E**) The variation in spike current of the artificial neuron under the APR. (**F**) Illustration of image preprocessing leveraging the APR and an artificial neuromorphic vision system using an artificial neural network for image recognition; 150% Gaussian noise is intentionally added to the input image. (**G**) Comparisons of the image recognition rate with and without image preprocessing based on the APR. (**H**) Confusion matrix of recognition results after preprocessing. (**I**) Dynamic vehicle imaging simulation detection results of one frame without and with the APR under uneven illumination (frame no. 18). (**J**) The confidence scatterplots of different exposure conditions with and without the APR according to each simulated image.

The human PLR completes in 0.2 to 1.5 s (*56*, *57*), ensuring high light adaptability, whereas the LM-based bionic pupil achieved full dilation in as fast as ~0.42 s (fig. S18D). Now, advanced driver assistance systems (ADASs) use photodetectors capable of recording 30 to 45 frames per second with response times of less than 16.7 ms (*58*). In comparison, human retinal photoreceptors exhibit response times ranging from 40 to 150 ms (*7*). In this work, our hemispherical photodetector demonstrated a minimum response time of ~13 ms (fig. S11), approaching commercial standards. However, commercial ADASs lack hardware for dynamic light adjustment, which explains their faster processing times. The total processing time of the APR system, encompassing both optical adjustment

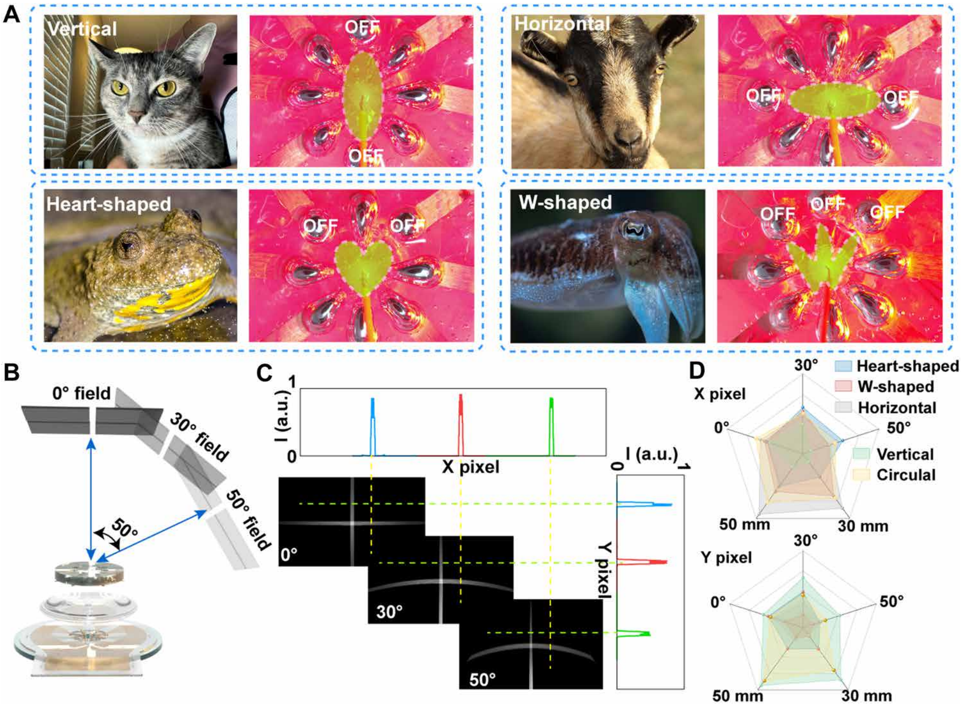

Fig. 6. Bioinspired APRs of various animal species. (**A**) Tunable artificial pupils compared with pupil shapes in a variety of animals. (**B**) Schematic illustration of the simulation setup describes two objects positioned at the object distance of 50 mm from 0°, 30°, and 50° fields, respectively. (**C**) The simulation results of target imaging with a heart-shaped pupil at three different FoV positions: 0°, 30°, and 50°, along with intensity graphs perpendicular to the parallel direction in the simulated images. (**D**) The radar chart compares the variation in intensity values of simulated images in both the vertical and parallel directions for circular, heart-shaped, horizontal, vertical, and W-shaped pupils at three different FoV positions (0°, 30°, and 50°) and difference distance from lens to retina (L = 30 and 50 mm); the focal length is 40 mm.

(PLR) and photoelectric response (photoreceptor), was completed in 0.5 s. The overall comparison of the three visual systems is presented in table S1. Although this speed remains insufficient for real-time driving applications, substantial opportunities remain for further optimization through dimensional scaling and architectural refinement of the system components.

Programmable bioinspired APRs for various animal species

The diverse pupillary reflex activities across animal species are shaped by their distinct habitats and ecological niches, which are visually manifested in variations in pupil shape. In our artificial pupil system, the dilation and constriction of the pupil are independently managed through an LM actuator positioned at eight distinct locations. This configuration enables precise adjustments of switch states in each branch, thereby allowing for programmable modifications to the pupil's shape, as illustrated in Fig. 6A; see figs. S32 and S33 for detailed structural images and shape configuration circuit. For example, the vertical pupil of a cat eye can be mimicked by deactivating the LM circuits at the upper and lower positions. Similarly, horizontal, heart-shaped, and W-shaped pupils can be broadly replicated.

To validate the tunability of the APR system, we used a ray-tracing method to simulate the imaging of different pupil shapes, including circular, heart-shaped, W-shaped, horizontal, and vertical pupils. Figure 6B presents a schematic illustration of the simulation setup, used to model the imaging of objects located 50 mm away at FoV positions of 0°, 30°, and 50°. The image-tracking results for various pupils are shown in Fig. 6C and fig. S34. The horizontally extended open region provides a clear image in the horizontal profile, allowing for a panoramic view, whereas the narrow upper region limits the vertical FoV. This configuration is beneficial for animals lower on the food chain, given that it helps them monitor their surroundings and detect potential threats in time to avoid predators, a critical survival strategy. A similar advantage is observed in animals with horizontal pupils, such as sheep. However, animals with vertical pupils, such as cats, can maintain a blurred vertical background while focusing on their target, enabling precise hunting. In addition, similar conclusions can be drawn by ray-tracing simulation results of DoF. For animals at lower trophic levels with heart-shaped, W-shaped, or parallel pupils, a greater DoF along the *x* axis was observed, whereas apex predators exhibit a larger DoF along the *y* axis, as mutually corroborated by experimental and simulation results (figs. S35 and S36). More details about the imaging contrast of the circular, heart-shaped, W-shaped, horizontal, and vertical pupils are provided in Fig. 6D, which closely aligns with the characteristics of biological pupils (*1*), demonstrating the feasibility and potential of this APR system in bioinspired pupil simulation.

DISCUSSION

Biological visual systems exhibit extraordinary imaging capabilities, namely, wide FoV and ultrahigh resolution, along with adaptive feedback mechanisms, offering substantial insights for research in artificial vision technologies and neuromorphic electronics. To date, extensive studies have been conducted on the components and systems of bionic eyes, including artificial synapses, artificial compound eyes, and optoelectronic neurons, all of which have accelerated the rapid development of artificial vision systems. However, most of these studies focused primarily on visual imaging itself, with limited attention given to bionic studies of neural feedback and PLR activities. The autonomously adaptive artificial vision system reported here draws inspiration from the pupillary reflex of biological visual systems. This system uses a hemispherical array of photodetectors to provide a wide FoV and adjusts the deformation of LM through photoelectric feedback to achieve bioinspired APRs, which enhances the accuracy of image recognition in environments with uneven exposure. This system exhibits strong plasticity and has substantial potential to mimic the PLRs of multiple species.

The bionic value of various animal pupil shapes lies in their ability to optimize the adaptability and functionality of artificial vision systems by mimicking the pupil morphologies of different species. The pupil shapes of animals vary according to their ecological environment and survival needs, providing essential references for the design of artificial vision systems. Therefore, our research not only enhances the visual performance of artificial vision systems but also strengthens their adaptability in dynamic environments, with particularly

PHOTO CREDITS: CAT EYE, COURTESY OF K.L.; HUMAN EYE, SHEEP EYE, AND *BOMBINA VARIEGATE* EYE, PIXABAY; CUTTLEFISH EYE IMAGE, PEXELS.

important application potential in fields such as bionic robots, autonomous driving, and machine vision. Furthermore, this vision system retains superior scalability and tunability. Through structural design, it can construct bionic vision systems in rectangular, triangular, or multicamera collaborative configurations to meet the specialized needs of industries such as industrial inspection, medical imaging, and intelligent transportation (fig. S37). However, the introduction of mechanical systems such as LM still leaves room for further improvements in system stability, response time, and efficiency. In addition, the programmability and deeper advantages of bionic mimicking of different pupil shapes have yet to be fully explored. Nevertheless, this APR technology holds substantial promise to further the exploration of bioinspired eyes and expand the capability into broad applications.

MATERIALS AND METHODS

Materials

All materials were commercially available without further purification. Y6 (BTPTT-4F), indium nitrate hydrate [In $(NO_3)_3{\cdot}xH_2O$, Sigma-Aldrich, 99.99%], and trichloromethane ($CHCl_3$, ≥99.8%) were purchased from Sigma-Aldrich. 2-Methoxyethanol (2-ME; 99.3%), acetylacetone (AcAc; 99%), and ammonium hydroxide ($NH_3{\cdot}H_2O$; 28%) were purchased from Alfa Aesar. Ecoflex (0030) was purchased from Smooth-On. PDMS (Sylgard 184) was purchased from Dow Corning Corporation. The EGaIn (gallium-indium eutectic alloys, 75.5 wt % gallium and 24.5 wt % indium) was purchased from Shanghai Mifang Science and Technology Co. Ltd.

Fabrication of photodetector arrays

A parylene layer (≈ 2 μm) was deposited by chemical vapor deposition (Specialty Coating Systems Inc.) on a surfactant-treated SiO_2 wafer substrate. The precursor solution of In_2O_3 (0.1 M) was prepared via dissolving In $(NO_3)_3{\cdot}xH_2O$ in 2-ME. AcAc and $NH_3{\cdot}H_2O$ solution with the same molar concentration were added as additives to facilitate exothermic combustion reaction. The mixture was stirred at room temperature for 24 hours before use. The In_2O_3 precursor was spin-coated on ultraviolet-ozone (UV-O_3)–treated substrate for 30 s at 3000 rpm/min and then followed by 1 min prebake at 100°C. The In_2O_3 active layers were defined by standard photolithography and wet etching with diluted hydrochloric acid (1:10 in water, v:v) followed by annealing at 220°C for 1 hour in the air. Next, Y6 solution was spin-coated on the substrate at 2000 rpm/min for 30 s, baked at 100°C for 10 min, and patterned by plasma dry etching. The Cr/Au (10/100 nm) electrodes were sputtered and patterned by photolithography and lift-off process. Then, a layer of 3-μm SU8 was deposited as an encapsulation layer. Last, a dry etching process was used to pattern the parylene substrate, and the entire photodetector array was peeled off from the SiO_2 substrate.

Device characterization and measurement

All measurements were performed under ambient conditions. The transmittance and absorbance spectra were measured using a UV-vis spectrophotometer (UV-2700, Shimadzu). The thickness values of In_2O_3 and Y6 films were measured by AFM (Bruker Dimension ICON). Electrical characteristics were performed by a semiconductor parameter analyzer (4200A-SCS, Keithley; 2636B, Keithley). The devices were illuminated by monochromatic light from different light-emitting diodes (365, 450, 520, 650, and 780 nm), driven by a signal generator (ATG2021H, Aigtek). The light intensity was measured using a standard silicon photodiode (S120VC, Thorlabs). UPS measurements were performed by an ESCALAB 250Xi x-ray photoelectron spectroscopy (Thermo Fisher Scientific, USA). UPS used the He I (21.22 eV) as the excitation source with an energy resolution of 50 meV.

Fabrication of hemispherical artificial retina

First, an Ecoflex substrate with an 8-cm diameter was prepared with a small hole of ~1.0-cm diameter in the center. Then, the Ecoflex substrate was uniformly stretched around the edges until the hole diameter reached ~2.0 cm. The flexible optoelectronic array was then attached to the stretched Ecoflex substrate and secured with Ecoflex. Upon release of the tensile force, the stretched Ecoflex returned to its initial state, causing the photodetector array to bend into a hemispherical shape.

Construction of artificial pupils

A PDMS module with a thickness of 0.5 cm and a diameter of 3 cm was prepared with a mold. Laser cutting was then used to shape the PDMS into a petal-shaped well, each filled with 0.5 M NaOH solution. Copper electrodes were attached to the bottom edge of each petal, and EGaIn was placed on top of each electrode. A platinum (Pt) electrode was inserted at the center of the petal-shaped well, serving as the anode and cathode, respectively. The LM expanded in the petal-shaped well.

Optical simulations for adaptive pupils

Optical simulations were performed using commercial ray-tracing software (OpticStudio 2023 R1.00, Radiant ZEMAX LLC, USA), and the optical simulations were performed in the sequential mode. The input wavelengths were selected in the visible spectrum (486, 588, and 656 nm). The shapes of the artificial pupils were optimized through design, with a 2D layout generated using computer-aided design software. Coordinate data were extracted to convert the design into aperture shapes, resulting in the fabrication of five different pupil apertures. The designed artificial vision system had a focal length of 4.0 cm.

Statistical analysis

We used SDs to quantify the bending stability of single-pixel photodetectors in fig. S13C ($N = 5$). The fitted line plot in fig. S12B was made using Origin 2024.

Supplementary Materials

The PDF file includes:
Methods
Figs. S1 to S37
Table S1

Other Supplementary Material for this manuscript includes the following:
Movies S1 and S2
Data file S1

REFERENCES AND NOTES

1. M. S. Banks, W. W. Sprague, J. Schmoll, J. A. Q. Parnell, G. D. Love, Why do animal eyes have pupils of different shapes? *Sci. Adv.* **1**, e1500391 (2015).
2. M. F. Land, D.-E. Nilsson, *Animal Eyes* (Oxford Univ. Press, ed. 2, 2012).
3. Y. M. Song, Y. Xie, V. Malyarchuk, J. Xiao, I. Jung, K.-J. Choi, Z. Liu, H. Park, C. Lu, R.-H. Kim, R. Li, K. B. Crozier, Y. Huang, J. A. Rogers, Digital cameras with designs inspired by the arthropod eye. *Nature* **497**, 95–99 (2013).
4. G. J. Lee, C. Choi, D.-H. Kim, Y. M. Song, Bioinspired artificial eyes: Optic components, digital cameras, and visual prostheses. *Adv. Funct. Mater.* **28**, 1705202 (2017).

5. M. Kim, G. J. Lee, C. Choi, M. S. Kim, M. Lee, S. Liu, K. W. Cho, H. M. Kim, H. Cho, M. K. Choi, N. Lu, Y. M. Song, D.-H. Kim, An aquatic-vision-inspired camera based on a monocentric lens and a silicon nanorod photodiode array. *Nat. Electron.* **3**, 546–553 (2020).
6. M. Lee, G. J. Lee, H. J. Jang, E. Joh, H. Cho, M. S. Kim, H. M. Kim, K. M. Kang, J. H. Lee, M. Kim, H. Jang, J.-E. Yeo, F. Durand, N. Lu, D.-H. Kim, Y. M. Song, An amphibious artificial vision system with a panoramic visual field. *Nat. Electron.* **5**, 452–459 (2022).
7. L. Gu, S. Poddar, Y. Lin, Z. Long, D. Zhang, Q. Zhang, L. Shu, X. Qiu, M. Kam, A. Javey, Z. Fan, A biomimetic eye with a hemispherical perovskite nanowire array retina. *Nature* **581**, 278–282 (2020).
8. D. Jayachandran, A. Oberoi, A. Sebastian, T. H. Choudhury, B. Shankar, J. M. Redwing, S. Das, A low-power biomimetic collision detector based on an in-memory molybdenum disulfide photodetector. *Nat. Electron.* **3**, 646–655 (2020).
9. M. S. Kim, M. S. Kim, M. Lee, H. J. Jang, D. H. Kim, S. Chang, M. Kim, H. Cho, J. Kang, C. Choi, J. P. Hong, D. K. Hwang, G. J. Lee, D.-H. Kim, Y. M. Song, Feline eye–inspired artificial vision for enhanced camouflage breaking under diverse light conditions. *Sci. Adv.* **10**, eadp2809 (2024).
10. M. Kim, S. Chang, M. Kim, J.-E. Yeo, M. S. Kim, G. J. Lee, D.-H. Kim, Y. M. Song, Cuttlefish eye–inspired artificial vision for high-quality imaging under uneven illumination conditions. *Sci. Robot.* **8**, eade4698 (2023).
11. C. Choi, G. J. Lee, S. Chang, Y. M. Song, D.-H. Kim, Inspiration from visual ecology for advancing multifunctional robotic vision systems: Bio-inspired electronic eyes and neuromorphic image sensors. *Adv. Mater.* **36**, e2412252 (2024).
12. J. Park, M. S. Kim, J. Kim, S. Chang, M. Lee, G. J. Lee, Y. M. Song, D.-H. Kim, Avian eye–inspired perovskite artificial vision system for foveated and multispectral imaging. *Sci. Robot.* **9**, eadk6903 (2024).
13. Y. Zhou, Z. Sun, Y. Ding, Z. Yuan, X. Qiu, Y. B. Cao, Z. Wan, Z. Long, S. Poddar, S. Kumar, W. Ye, C. L. J. Chan, D. Zhang, B. Ren, Q. Zhang, H. S. Kwok, M. G. Li, Z. Fan, An ultrawide field-of-view pinhole compound eye using hemispherical nanowire array for robot vision. *Sci. Robot.* **9**, eadi8666 (2024).
14. X. Zhao, H. Zou, M. Wang, J. Wang, T. Wang, L. Wang, X. Chen, Conformal neuromorphic bioelectronics for sense digitalization. *Adv. Mater.* **36**, e2403444 (2024).
15. C. Choi, J. Leem, M. S. Kim, A. Taqieddin, C. Cho, K. W. Cho, G. J. Lee, H. Seung, H. J. Bae, Y. M. Song, T. Hyeon, N. R. Aluru, S. Nam, D.-H. Kim, Curved neuromorphic image sensor array using a MoS_2-organic heterostructure inspired by the human visual recognition system. *Nat. Commun.* **11**, 5934 (2020).
16. F. Liao, Z. Zhou, B. J. Kim, J. Chen, J. Wang, T. Wan, Y. Zhou, A. T. Hoang, C. Wang, J. Kang, J.-H. Ahn, Y. Chai, Bioinspired in-sensor visual adaptation for accurate perception. *Nat. Electron.* **5**, 84–91 (2022).
17. T.-J. Lee, K.-R. Yun, S.-K. Kim, J.-H. Kim, J. Jin, K.-B. Sim, D.-H. Lee, G. W. Hwang, T.-Y. Seong, Realization of an artificial visual nervous system using an integrated optoelectronic device array. *Adv. Mater.* **33**, e2105485 (2021).
18. J. Y. O. Y. Lee, W. Xu, O. Kim, T. R. Kim, J. Kang, Y. Kim, D. Son, J. B.-H. Tok, M. J. Park, Z. Bao, T.-W. Lee, Stretchable organic optoelectronic sensorimotor synapse. *Sci. Adv.* **4**, eaat7387 (2018).
19. L. Sun, Y. Du, H. Yu, H. Wei, W. Xu, W. Xu, An artificial reflex arc that perceives afferent visual and tactile information and controls efferent muscular actions. *Research* **2022**, 1–11 (2022).
20. S. Kim, D. G. Roe, Y. Y. Choi, H. Woo, J. Park, J. I. Lee, Y. Choi, S. B. Jo, M. S. Kang, Y. J. Song, S. Jeong, J. H. Cho, Artificial stimulus-response system capable of conscious response. *Sci. Adv.* **7**, eabe3996 (2021).
21. J. Gong, H. Wei, J. Liu, L. Sun, Z. Xu, H. Huang, W. Xu, An artificial visual nerve for mimicking pupil reflex. *Matter* **5**, 1578–1589 (2022).
22. B. Dang, K. Liu, X. Wu, Z. Yang, L. Xu, Y. Yang, R. Huang, One-phototransistor-one-memristor array with high-linearity light-tunable weight for optic neuromorphic computing. *Adv. Mater.* **35**, e2204844 (2022).
23. K. Lee, H. Han, Y. Kim, J. Park, S. Jang, H. Lee, S. W. Lee, H. Kim, Y. Kim, T. Kim, D. Kim, G. Wang, C. Park, Retina-inspired structurally tunable synaptic perovskite nanocones. *Adv. Funct. Mater.* **31**, 2105596 (2021).
24. C. Jo, J. Kim, J. Y. Kwak, S. M. Kwon, J. B. Park, J. Kim, G.-S. Park, M.-G. Kim, Y.-H. Kim, S. K. Park, Retina-inspired color-cognitive learning via chromatically controllable mixed quantum dot synaptic transistor arrays. *Adv. Mater.* **34**, 2108979 (2022).
25. D. Li, H. Ren, Y. Chen, Y. Tang, K. Liang, Y. Wang, F. Li, G. Liu, L. Meng, B. Zhu, Bidirectionally photoresponsive optoelectronic transistors with dual photogates for all-optical-configured neuromorphic vision. *Adv. Funct. Mater.* **33**, 2303198 (2023).
26. T. Xie, Q. Wang, M. Li, Y. Fang, G. Li, S. Shao, W. Yu, S. Wang, W. Gu, C. Zhao, M. Tang, J. Zhao, Carbon nanotube optoelectronic synapse transistor arrays with ultra-low power consumption for stretchable neuromorphic vision systems. *Adv. Funct. Mater.* **33**, 2303970 (2023).
27. Z. Rao, Y. Lu, Z. Li, K. Sim, Z. Ma, J. Xiao, C. Yu, Curvy, shape-adaptive imagers based on printed optoelectronic pixels with a kirigami design. *Nat. Electron.* **4**, 513–521 (2021).
28. M. R. Khan, C. B. Eaker, E. F. Bowden, M. D. Dickey, Giant and switchable surface activity of liquid metal via surface oxidation. *Proc. Natl. Acad. Sci. U.S.A.* **111**, 14047–14051 (2014).
29. M. Song, K. E. Daniels, A. Kiani, S. Rashid-Nadimi, M. D. Dickey, Interfacial tension modulation of liquid metal via electrochemical oxidation. *Adv. Intell. Syst.* **3**, 2100024 (2021).
30. C. B. Eaker, M. D. Dickey, Liquid metal actuation by electrical control of interfacial tension. *Appl. Phys. Rev.* **3**, 031103 (2016).
31. J. Wissman, M. D. Dickey, C. Majidi, Field-controlled electrical switch with liquid metal. *Adv. Sci.* **4**, 1700169 (2017).
32. D. Li, J. Du, Y. Tang, K. Liang, Y. Wang, H. Ren, R. Wang, L. Meng, B. Zhu, Y. Li, Flexible and air-stable near-infrared sensors based on solution-processed inorganic–organic hybrid phototransistors. *Adv. Funct. Mater.* **31**, 2105887 (2021).
33. J. Kim, S.-M. Kwon, Y. K. Kang, Y.-H. Kim, M.-J. Lee, K. Han, A. Facchetti, M.-G. Kim, S. K. Park, A skin-like two-dimensionally pixelized full-color quantum dot photodetector. *Sci. Adv.* **5**, eaax8801 (2019).
34. K. Liang, R. Wang, B. Huo, H. Ren, D. Li, Y. Wang, Y. Tang, Y. Chen, C. Song, F. Li, B. Ji, H. Wang, B. Zhu, Fully printed optoelectronic synaptic transistors based on quantum dot-Metal oxide semiconductor heterojunctions. *ACS Nano* **16**, 8651–8661 (2022).
35. J. Kim, C. Jo, M.-G. Kim, G.-S. Park, T. J. Marks, A. Facchetti, S. K. Park, Vertically stacked full color quantum dots phototransistor arrays for high-resolution and enhanced color-selective imaging. *Adv. Mater.* **34**, e2106215 (2021).
36. A. Bochkovskiy, C.-Y. Wang, H.-Y. M. Liao, YOLOv4: Optimal speed and accuracy of object detection. arXiv:2004.10934 [cs.CV] (2020).
37. M.-K. Kim, J.-S. Lee, Synergistic improvement of long-term plasticity in photonic synapses using ferroelectric polarization in hafnia-based oxide-semiconductor transistors. *Adv. Mater.* **32**, 1907826 (2020).
38. M. Lee, W. Lee, S. Choi, J. W. Jo, J. Kim, S. K. Park, Y.-H. Kim, Brain-inspired photonic neuromorphic devices using photodynamic amorphous oxide semiconductors and their persistent photoconductivity. *Adv. Mater.* **29**, 1604310 (2017).
39. W. Qiu, Y. Huang, L. A. Kong, Y. Chen, W. Liu, Z. Wang, J. Sun, Q. Wan, J. H. Cho, J. Yang, Y. Gao, Optoelectronic In-Ga-Zn-O memtransistors for artificial vision system. *Adv. Funct. Mater.* **30**, 2002325 (2020).
40. L. Dou, Y. M. Yang, J. You, Z. Hong, W.-H. Chang, G. Li, Y. Yang, Solution-processed hybrid perovskite photodetectors with high detectivity. *Nat. Commun.* **5**, 5404 (2014).
41. J. Zhang, Q. Shi, R. Wang, X. Zhang, L. Li, J. Zhang, L. Tian, L. Xiong, J. Huang, Spectrum-dependent photonic synapses based on 2D imine polymers for power-efficient neuromorphic computing. *InfoMat* **3**, 904–916 (2021).
42. M. Song, K. Kartawira, K. D. Hillaire, C. Li, C. B. Eaker, A. Kiani, K. E. Daniels, M. D. Dickey, Overcoming rayleigh-plateau instabilities: Stabilizing and destabilizing liquid-metal streams via electrochemical oxidation. *Proc. Natl. Acad. Sci. U.S.A.* **117**, 19026–19032 (2020).
43. Y. Yang, Y. Shen, A liquid metal-based module emulating the intelligent preying logic of flytrap. *Nat. Commun.* **15**, 3398 (2024).
44. D. D. Li, Q. Wang, J. Liu, A tunable liquid metal electronic oscillator as a DC-AC converter. *Soft Matter* **18**, 5185–5193 (2022).
45. S. Handschuh-Wang, Y. Chen, L. Zhu, T. Gan, X. Zhou, Electric actuation of liquid metal droplets in acidified aqueous electrolyte. *Langmuir* **35**, 372–381 (2019).
46. J. Tang, X. Zhao, J. Li, Y. Zhou, J. Liu, Liquid metal phagocytosis: Intermetallic wetting induced particle internalization. *Adv. Sci.* **4**, 1700024 (2017).
47. B. Yuan, L. Wang, X. Yang, Y. Ding, S. Tan, L. Yi, Z. He, J. Liu, Liquid metal machine triggered violin-like wire oscillator. *Adv. Sci.* **3**, 1600212 (2016).
48. J. Shu, D.-A. Ge, E. Wang, H. Ren, T. Cole, S. Y. Tang, X. Li, X. Zhou, R. Li, H. Jin, W. Li, M. D. Dickey, S. Zhang, A liquid metal artificial muscle. *Adv. Mater.* **33**, e2103062 (2021).
49. D.-D. Li, T.-Y. Liu, J. Ye, L. Sheng, J. Liu, Liquid metal-enabled soft logic devices. *Adv. Intell. Syst.* **3**, 2000246 (2021).
50. Y. He, J. You, M. D. Dickey, X. Wang, Liquid-metal transfer from an anode to a cathode without short circuiting. *Nat. Chem. Eng.* **1**, 293–300 (2024).
51. C. Yang, I. Choi, H. Jung, D. T. Park, H. K. Choi, Y. Chung, Cryogenic transimpedance amplifier based on a commercial operational amplifier. *J. Korean Phys. Soc.* **83**, 549–555 (2023).
52. R. J. Lucas, S. Hattar, M. Takao, D. M. Berson, R. G. Foster, K.-W. Yau, Diminished pupillary light reflex at high irradiances in melanopsin-knockout mice. *Science* **299**, 245–247 (2003).
53. E. L. Markwell, B. Feigl, A. J. Zele, Intrinsically photosensitive melanopsin retinal ganglion cell contributions to the pupillary light reflex and circadian rhythm. *Clin. Exp. Optom.* **93**, 137–149 (2010).
54. International Electrotechnical Commission, *Photobiological Safety of Lamps and Lamp Systems* IEC 62471 (IEC, 2006).
55. R. Khanam, M. Hussain, What is YOLOv5: A deep look into the internal features of the popular object detector. arXiv:2407.20892v1 [cs.CV] (2024).
56. S. Mathôt, Pupillometry: Psychology, physiology, and function. *J. Cogn.* **1**, 16 (2018).
57. J. J. Gooley, I. Ho Mien, M. A. St Hilaire, S.-C. Yeo, E. C.-P. Chua, E. van Reen, C. J. Hanley, J. T. Hull, C. A. Czeisler, S. W. Lockley, Melanopsin and rod-cone photoreceptors play different roles in mediating pupillary light responses during exposure to continuous light in humans. *J. Neurosci.* **32**, 14242–14253 (2012).

58. D. Gehrig, D. Scaramuzza, Low-latency automotive vision with event cameras. *Nature* **629**, 1034–1040 (2024).

Acknowledgments: This work was performed in part at the Chapel Hill Analytical and Nanofabrication Laboratory (CHANL), a member of the North Carolina Research Triangle Nanotechnology Network (RTNN), which is supported by the NSF, grant ECCS-2025064, as part of the National Nanotechnology Coordinated Infrastructure (NNCI). We thank the Westlake Centre for Micro/Nano Fabrication, the Instrumentation and Service Centre for Physical Sciences (ISCPS), and the Instrumentation and Service Centre for Molecular Sciences (ISCMS) at Westlake University for facility support and technical assistance. **Funding:** This work was supported by the fund from NSF CAREER Award (ECCS-2443105) and AGILE grants from UNC Institute for Convergent Science. Research reported in this publication was also supported by the National Institute of Biomedical Imaging and Bioengineering at the NIH under award number 1R01EB034332-03. **Author contributions:** K.L., R.W., A.Z., B.Z., and W.B. designed the experiments, analyzed the data, and wrote the paper. K.L., Y. Wu, Z.Z., and Y. Wang fabricated the photodetector array and performed characterization of individual devices. K.L. and Y. Wu fabricated the LM logical module and LM actuators. G.L., S.X., and Y.L. designed the control and integrated the circuits. K.L. and A.Z. performed the characterizations for In_2O_3 and Y6 films. K.L. and Y. Wu performed the theoretical and experimental optics. K.L. and R.W. developed the SNN and delivered related image recognition. A.Z., W.X., M.D.D., B.Z., and W.B. revised the manuscript. All authors discussed the results and commented on the manuscript. **Competing interests:** The authors declare that they have no competing interests. **Data, code, and materials availability:** All materials were commercially available. All data needed to support the conclusions of this manuscript are included in the main text or Supplementary Materials. The data for this study have been deposited in the Dryad database (https://doi.org/10.5061/dryad.7d7wm388z).

Submitted 27 February 2025
Accepted 14 January 2026
Published 11 February 2026
10.1126/scirobotics.adx0715

Science Robotics

Bioinspired adaptive pupil reflex based on liquid-metal shape-shifters for machine vision

Kun Liang, Rui Wang, Gavin Lyda, Anran Zhang, Wanrong Xie, Yihang Wang, Sicheng Xing, Yizhang Wu, Zhibo Zhang,
Yihan Liu, Michael D. Dickey, Bowen Zhu, and Wubin Bai

Sci. Robot. **11** (111), eadx0715. DOI: 10.1126/scirobotics.adx0715

Science Robotics (ISSN 2470-9476) is published by the American Association for the Advancement of Science. 1200 New York Avenue NW, Washington, DC 20005. The title *Science Robotics* is a registered trademark of AAAS.